Journal of *Marine Science and Engineering*

MDPI

Article

Resistance and Seakeeping Performance Assessment of a Coastal Fishing Vessel Based on Reverse Engineering with a 3D Laser Scanner

Mingchen Ma [1], Samkyung Sung [2], Jungkeun Oh [1], Sooyeon Kwon [2,*] and Daewon Seo [1,*]

[1] Department of Naval Architecture and Ocean Engineering, Kunsan National University, Gunsan 54151, Republic of Korea
[2] Fishing Vessel Safety Research Task Force, Korea Maritime Transportation Safety Authority (KOMSA), Sejong 30100, Republic of Korea
* Correspondence: kissiny@komsa.or.kr (S.K.); dwseo@kunsan.ac.kr (D.S.); Tel.: +82-44-330-2575 (S.K.); +82-63-469-1858 (D.S.)

Abstract

Korean coastal fishing vessels are built from shipyard-owned fiber-reinforced plastic molds without standardized drawings, so hull forms differ within a tonnage class and geometry data are scarce. This study presents a stepwise reverse-engineering procedure with stage checks that converts terrestrial three-dimensional laser scans of molds and hulls into analysis-ready models for assessing resistance, seakeeping and operability. In a 21-vessel sample drawn from 2391 vessels built in 2023–2025, the length–beam ratio differed by up to 1.49 within a class. For a 3 gross ton class target vessel, Reynolds-averaged Navier–Stokes simulations with the volume-of-fluid method at three speeds gave the largest total resistance coefficient at a length Froude number of 0.516, with pressure resistance contributing 85–91%. Frequency-domain panel-method analyses of 63 seakeeping conditions showed that roll remained within the operational limit owing to the large metacentric height and assumed roll damping, whereas lateral acceleration, deck wetness and slamming exceeded their limits in some conditions. The operability of the target vessel is therefore governed not by roll but by the lateral acceleration at the wheelhouse, arising mainly from sway and yaw, and by the bow relative motion over the low deck. Hull-specific limits derived from measured geometry can complement tonnage-based departure restrictions.

Keywords: coastal fishing vessel; 3D laser scanning; reverse engineering; resistance; seakeeping; operability

Check for updates

Academic Editor: Decheng Wan

Received: 27 October 2026
Revised: 16 November 2026
Accepted: 17 November 2026
Published: 25 November 2026

Copyright: © 2026 by the authors. Licensee MDPI, Basel, Switzerland. This article is an open access article distributed under the terms and conditions of the Creative Commons Attribution (CC BY) license.

1. Introduction

Coastal fishing vessels in Korea are not mass-produced to standard designs. Instead, small shipyards build them one at a time from their own fiber-reinforced plastic (FRP) molds, adapting each hull to the owner's requirements. Under this practice, verification of resistance and seakeeping performance is generally not required at the design stage, and modifications such as the addition of buoyancy along the hull sides are also made after construction. As a result, fishing vessels registered in the same tonnage class differ in their principal dimensions and hull forms.

Fishing vessels of less than 10 gross tons (GT) account for approximately 95% of the fishing vessels registered in Korea [1]. Of the vessels involved in collisions in 2023–2024, approximately 67.3% were fishing vessels and approximately 51.1% were small vessels

of less than 20 GT [2]. The operational safety of small fishing vessels currently depends mainly on marine weather warnings, such as wind–wave advisories, and on departure restrictions classified by gross tonnage and time period [3]; these measures do not account for differences in performance in waves that arise from hull form within the same tonnage range. Because the motion characteristics of fishing vessels in waves vary considerably with vessel size and speed [4], the current criteria need to be supplemented on the basis of hull-specific performance.

Performance-based safety management requires hull geometry data; however, lines plans or three-dimensional (3D) geometry data are often unavailable for small FRP fishing vessels. Reverse engineering based on 3D scanning can fill this gap and has been applied to the geometry and weight quality control of composite small craft [5] and to the construction of a digital model of an 8 m class small craft [6]. Terrestrial laser scanning and close-range photogrammetry have also been used to document the as-built geometry of boat and ship hulls [7,8], and hull point clouds have been converted into curve networks and non-uniform rational B-spline (NURBS) surfaces [9]. Lovas et al. [10] described the survey geometry, the reflectivity problems and the point-cloud processing required to obtain hull surface models for hydrodynamic simulations. These studies concentrated mainly on the accuracy of the measurement and the reconstruction of the hull surface. No procedure has been established that covers the entire process from measurement to the generation of an analysis model, even though the measurement quality of large FRP molds in shipyard workshops is affected by their glossy finish and concave female surfaces. The seakeeping performance of small fishing vessels has been examined through motion responses in regular waves [4], marine-activity criteria based on operational and survival limits [1], and seakeeping performance indices for 16 fishing vessels [11]. Operability criteria for fishing vessels have also been formulated on the basis of motion-induced interruptions of the crew [12], the operability of small traditional fishing boats has been evaluated under different loading conditions [13], and the influence of hull-form parameters on seakeeping has been examined with a systematic hull series [14]. For resistance, Reynolds-averaged Navier–Stokes simulations with free-surface capturing have been verified and validated for planing hulls [15], applied to the calm-water resistance and running attitude of small hard-chine hulls [16] and validated against towing-tank tests for a fishing vessel [17], and Iqbal et al. [18] combined such simulations with response-surface methodology to optimize the hull form of a small fishing vessel for resistance and dynamic responses. These numerical studies used hull forms whose lines were known in advance. However, studies that evaluate resistance and seakeeping together from the measured geometry of an actual vessel and derive its operability limits remain scarce.

From these studies, three research gaps can be identified. First, previous scanning studies dealt mainly with measurement accuracy and surface reconstruction, and no procedure with explicit check items has been established that carries the scanned FRP molds and hulls of small fishing vessels through to analysis-ready models for hydrodynamic solvers. Second, the variation in hull forms within the same tonnage class of small fishing vessels, which motivates a hull-specific assessment, has not been quantified with data on newly built vessels. Third, resistance, seakeeping and operability have rarely been evaluated together for an actual small fishing vessel whose geometry is available only through measurement, so the responses that restrict its operation remain unclear.

This study has two objectives. The first is to establish a procedure, with check items defined for each stage, for acquiring the mold and hull geometry of existing coastal fishing vessels with a terrestrial 3D laser scanner and converting it into a computer-aided design (CAD) model suitable for analysis. The second is to demonstrate the applicability of this procedure by applying it to a 3 GT class coastal fishing vessel, estimating its resistance and

seakeeping performance, and deriving its operability limits. The new contributions of this study are threefold: (i) a scan-to-analysis procedure for the FRP molds and hulls of small fishing vessels in which check items are defined for each stage and corrective actions for the first three, so that the scanned geometry can be used directly in resistance and seakeeping analyses; (ii) a quantification of the within-class variation in the length–beam ratio, as an indicator of hull form, based on a 21-vessel sample drawn from recent construction surveys; and (iii) a complete chain from scanning to resistance, seakeeping and an operability map for a measured 3 GT class hull, showing that, for the assumed roll damping, the operability of this vessel, which has a large metacentric height, is governed by the lateral acceleration and the bow relative motion rather than by roll. Because the procedure requires neither lines plans nor 3D hull geometry data, it enables hull-specific performance data to be obtained for existing small fishing vessels, providing a technical basis for complementing tonnage-based safety measures. Section 2 describes the sampling design and the acquisition of hull geometry, Section 3 presents the hydrodynamic analysis methods, Section 4 discusses the results, and Section 5 summarizes the conclusions.

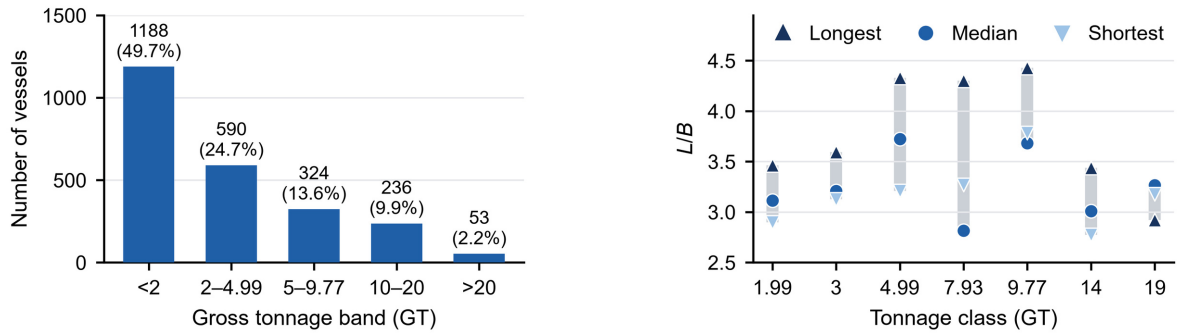
2. Sampling Design and Hull Geometry Acquisition

2.1. Sampling Design

The vessels to be measured were selected from a population of 2391 fishing vessels shorter than 24 m that passed construction survey in 2023–2025; the tonnage distribution of this population is shown in Figure 1a. Vessels below 2 GT accounted for 49.7% of the population, those of 2–4.99 GT for 24.7% and those of 5–9.77 GT for 13.6%, so that vessels below 10 GT made up about 88% of the total. The relationship between the registered length L (m) and the gross tonnage GT was approximated by $L = 4.17 \ln(\mathrm{GT}) + 5.51$, with a coefficient of determination R^2 of 0.910. Seven tonnage classes of 1.99, 3, 4.99, 7.93, 9.77, 14 and 19 GT were defined, and the longest, median and shortest vessels by registered length were identified in each class, giving the sample of 21 vessels listed in Table 1. The median-length vessel was taken to represent the standard hull form of its class, whereas the longest and shortest vessels indicate the range of hull-form variation within the class. To allow hull forms of different lengths to be compared directly, seven vessels were then selected from this sample for scanning and hydrodynamic analysis. Six of them, the longest, median and shortest vessels of the 3 GT and 4.99 GT classes, form length series within the same class, and the seventh, the median vessel of the 14 GT class, extends the comparison to a larger tonnage class. These seven vessels are referred to as the representative vessels. Because the sample was deliberately chosen to cover the length range within each class, it is not intended to reproduce the population distribution statistically; vessels above 20 GT, which make up 2.2% of the population, were not included.

Table 1. Registered length and breadth of the 21 sampled vessels.

Class (GT)	L (m) Max/Mid/Min	B (m) Max/Mid/Min	L/B Range
1.99	8.10/7.47/6.75	2.34/2.40/2.33	2.90–3.46
3	9.63/9.11/7.50	2.68/2.84/2.40	3.13–3.59
4.99	12.17/11.39/9.11	2.81/3.06/2.84	3.21–4.33
7.93	15.40/13.73/12.75	3.58/4.88/3.90	2.81–4.30
9.77	17.63/16.05/14.30	3.98/4.36/3.78	3.68–4.43
14	18.77/17.45/16.00	5.46/5.80/5.77	2.77–3.44
19	20.87/19.93/18.42	7.15/6.10/5.80	2.92–3.27



(**a**) (**b**)

Figure 1. Population and sample: (**a**) tonnage distribution of the 2391 fishing vessels shorter than 24 m that passed construction survey in 2023–2025; (**b**) length–beam ratio L/B of the longest, median and shortest sampled vessels in each tonnage class.

The registered lengths of the sampled vessels range from 6.75 to 20.87 m and their L/B ratios from 2.77 to 4.43. As shown in Figure 1b, L/B differs by 1.12 and 1.49 within the 4.99 GT and 7.93 GT classes, respectively, showing that hull-form characteristics vary substantially even within the same tonnage class. The engine power of the 14 GT class sample was about 26% higher than that of the 14 GT class vessels in the population, and because mold measurements depended on the cooperation of shipyards, the sample is concentrated on the southern coast of Korea and does not include vessels from the east coast. In Table 1, Max, Mid and Min denote the longest, median and shortest vessels of each class by registered length, and L/B is based on the registered length.

The registered dimensions of the seven representative vessels, taken from the construction survey records, are listed in Table 2. The registered length ranges from 7.50 to 9.63 m in the 3 GT class and from 9.11 to 12.17 m in the 4.99 GT class, with L/B ranging from 3.13 to 3.59 and from 3.21 to 4.33, respectively, so that the effect of length at nearly constant tonnage can be examined directly. This paper presents the results for the median-length vessel of the 3 GT class, which is hereafter referred to as the target vessel.

Table 2. Registered dimensions of the representative vessels selected for hull-form comparison.

Class (GT)	Length Rank	L (m)	B (m)	D (m)	L/B
3	Longest	9.63	2.68	0.75	3.59
3	Median	9.11	2.84	0.79	3.21
3	Shortest	7.50	2.40	0.88	3.13
4.99	Longest	12.17	2.81	0.79	4.33
4.99	Median	11.39	3.06	0.88	3.72
4.99	Shortest	9.11	2.84	0.84	3.21
14	Median	17.45	5.80	0.93	3.01

2.2. Field 3D Scanning

A FARO Focus Core 100 terrestrial laser scanner (FARO Technologies, Inc., Lake Mary, FL, USA) was used for the measurements, and FARO SCENE (version 2026.1.0), Geomagic Design X (version 2026.1.0) and Rhino 7 were used for post-processing and reverse engineering. As shown in Figure 2a, the scanner was mounted level on a tripod at least 1.5 m above the floor, at a height from which the entire object could be viewed, and its inclination indicator was checked before each scan. Scanning started amidships, with the scan station moved progressively toward the bow and the stern, and the resolution and quality settings were selected according to the size of the object and the required accuracy. Adjacent stations were arranged to share an overlap region and common targets

for registration, and additional or multi-level stations were used for the bottom and bow surfaces, which are prone to blind spots, and for large molds. Missing regions and target-recognition failures were checked on site before demobilization to reduce the need for re-scanning, and the data were copied to a backup medium before leaving the site. For hulls below 10 GT, a small number of stations is sufficient, although the bottom and bow surfaces require particular attention, whereas larger molds require more stations and a multi-level scan plan prepared in advance.

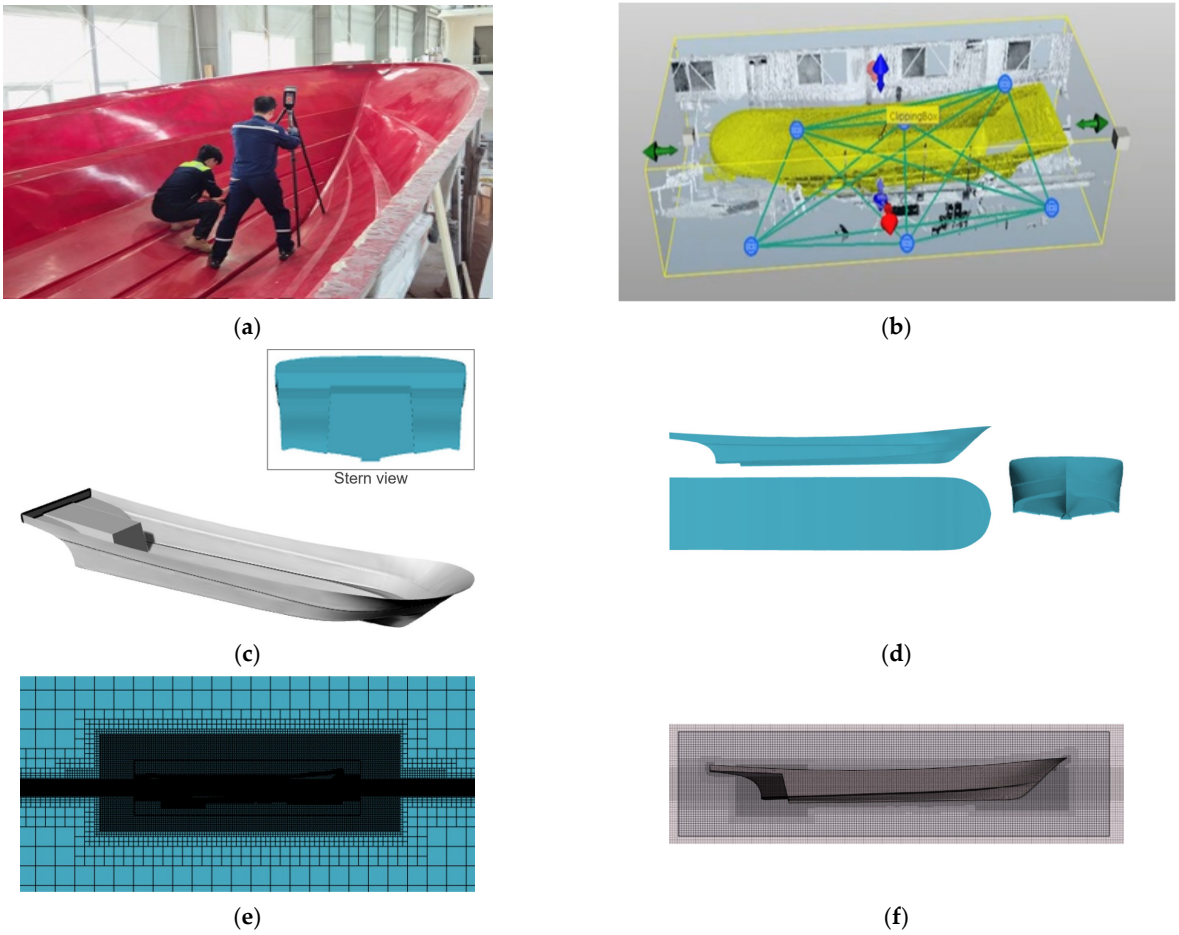


Figure 2. From field measurement to numerical models: (**a**) scanner set-up inside an FRP mold; (**b**) registered point cloud of a 4.99 GT class sample vessel; (**c**) reverse-engineered hull surface model of the target vessel with an inset stern view; (**d**) profile, plan and bow views of the model; (**e**) volume mesh in the center plane; (**f**) close-up of the mesh near the hull for STAR-CCM+.

When the measured object is an FRP mold, the inner surface of the mold corresponds to the outer surface of the hull, so the normals of the measured surface point in the direction opposite to those of the hull. Whether each object was a mold or a hull was therefore recorded, and for molds the surface orientation was reversed in the reverse-engineering stage. Moreover, because a mold does not reflect modifications made after construction, vessels with a modification history must be measured on the finished hull. In both cases, the scanned surface represents the outer surface of the hull, which is the only geometry required for the hydrodynamic analyses. Scanning a mold is often practical, because several hulls are built from the same mold and the mold can be accessed in the shipyard without lifting a vessel out of the water.

Because only the outer surface is required, the wall thickness of the hull was neither measured nor used in the present procedure, and the mass properties were set as described

in Section 2.5 rather than estimated from the structural weight of the hull. A terrestrial laser scanner records only the surfaces visible from the scan stations, so the thickness cannot be obtained from a single scanned surface; it could be estimated by combining the scans with ultrasonic thickness measurements at selected points or, where the inner surface is not hidden by the deck, fish holds and equipment, by registering scans of the outer and inner surfaces of a finished hull. Such data would allow a preliminary estimate of the hull weight and of the strength of the FRP hull, which also affects the safety of the vessel; this extension is left for future work.

2.3. Post-Processing and Stage Checks

Post-processing was performed in FARO SCENE in the sequence of data import, registration, noise removal, coordinate alignment, completeness check and CAD export; Figure 2b shows a registered point cloud. Registration was primarily target-based, and regions with insufficient targets were supplemented by cloud-to-cloud registration; when the registration error exceeded the tolerance, the data were re-registered or re-scanned. Scattered points caused by reflections and moving objects, as well as background points, were removed in stages, taking care that points on the hull surface were not deleted with them. The point cloud was then aligned to a standard coordinate system referenced to the hull centerline, the baseline, the forward perpendicular (F.P.) and the aft perpendicular (A.P.); this alignment governs the extraction of the principal dimensions and the definition of the attitude of the analysis model.

Points were removed only as far as needed to eliminate reflections, moving objects and background, and residual noise was accepted only at a level that did not hinder the subsequent reverse engineering; the point cloud was then exported in a CAD-compatible format and inspected in Geomagic Design X.

The check items of each stage and the corrective actions taken when the checks of the first three stages fail are summarized in Figure 3. When a problem in the data itself, such as missing geometry, is identified, the procedure returns to re-scanning on site.

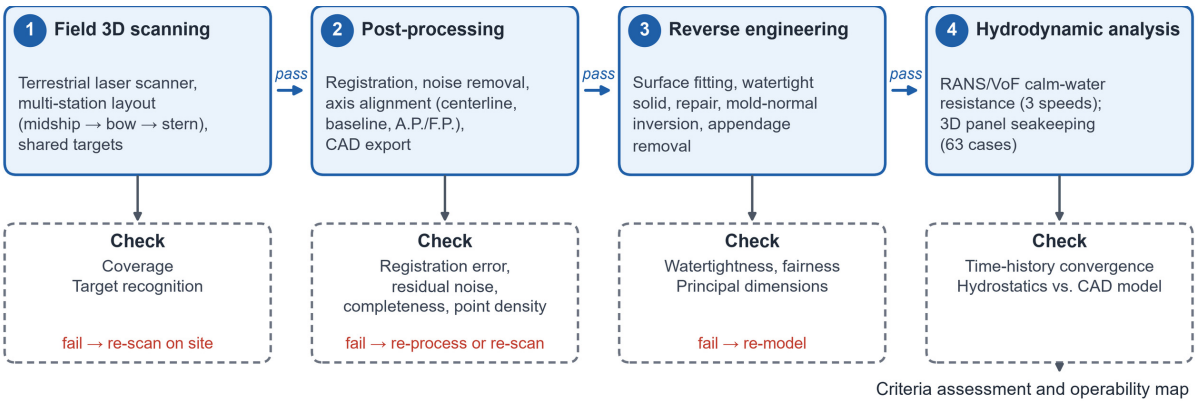


Figure 3. Measurement-to-analysis procedure with the check items of each stage and the corrective actions of the first three stages.

2.4. Reverse Engineering and Analysis Model

A point cloud has a non-uniform density and contains missing regions and residual noise, so it cannot be used directly as the watertight surface required for mesh generation. The post-processed point cloud was therefore reconstructed into surface and solid models in Geomagic Design X through region segmentation and surface fitting. For the target vessel, surface defects, residual surfaces and insufficient curvature in the bow region of the initial model were corrected in Rhino, and the stern appendages not needed for the

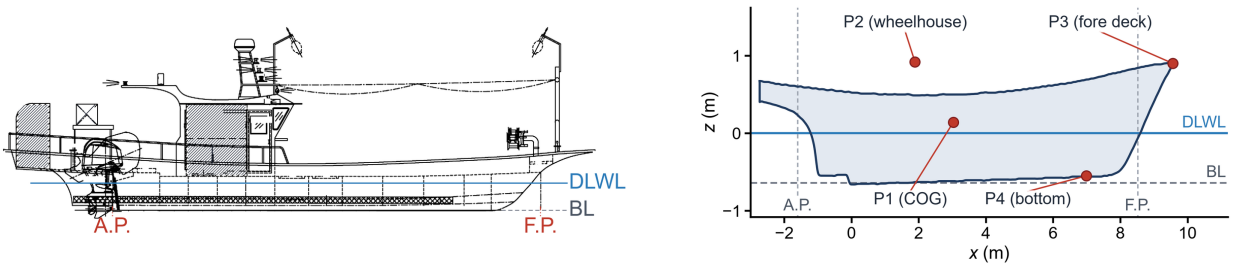
analysis were removed to finalize the analysis model shown in Figure 2c,d. The results presented hereafter therefore refer to the bare hull and exclude the effects of appendages and the propulsor.

2.5. Target Vessel

The target vessel, the median-length vessel of the 3 GT class in Table 2, is a small coastal fishing vessel equipped with an outboard motor. Its principal particulars and the hydrostatics of the reverse-engineered model are listed in Table 3, and the profile of the general arrangement and the response evaluation points are shown in Figure 4. The length overall of 14.00 m includes the outboard motor bracket at the stern, and the length between perpendiculars L_{BP} is 10.12 m; these lengths are defined on a different basis from the registered length of 9.11 m used in the sampling design. At a draft of 0.640 m, the displacement is 8.892 t, with $L_{BP}/B = 3.56$ and $B/T = 4.44$, indicating a wide hull with a shallow draft. In terms of the Froude number based on the length between perpendiculars, Fr_L, the analyzed speeds range from 0.26 to 0.77, extending from the displacement regime into the semi-displacement regime. The provided vertical center of gravity, KG = 0.779 m above the baseline, was used, and the longitudinal center of gravity was assumed to coincide with the longitudinal center of buoyancy (LCB).

Table 3. Principal particulars and hydrostatics of the target vessel on even keel at $T = 0.640$ m.

Item	Symbol	Value
Length overall (including outboard-motor bracket)	L_{OA}	14.00 m
Length between perpendiculars	L_{BP}	10.12 m
Breadth (molded)	B	2.84 m
Depth	D	0.790 m
Draft	T	0.640 m
Displaced volume	∇	8.675 m^3
Displacement	Δ	8.892 t
Wetted surface area	S	32.41 m^2
Longitudinal center of buoyancy (x)	LCB	3.029 m
Vertical center of buoyancy	KB	0.418 m
Transverse metacentric radius	BM	1.472 m
Vertical center of gravity	KG	0.779 m
Metacentric height	GM	1.111 m



(**a**) (**b**)

Figure 4. Target vessel: (**a**) profile of the general arrangement; (**b**) response evaluation points P1–P4.

In Table 3, the length overall, the length between perpendiculars, the breadth and the draft were taken from the general arrangement drawing, the depth from the construction survey record and KG from the value provided for the vessel; the displaced volume, displacement, wetted surface area, LCB, vertical center of buoyancy KB and transverse metacentric

radius BM were obtained from the reverse-engineered model, and the metacentric height was obtained as GM = KB + BM − KG. Figure 4b, the longitudinal center of buoyancy in Table 3 and the coordinates of the center of gravity and the response evaluation points given in Section 3 refer to the same hull coordinate system, in which x is positive forward, with the A.P. at $x = -1.60$ m and the F.P. at $x = 8.52$ m; $y = 0$ lies on the centerline, $z = 0$ corresponds to the design load waterline (DLWL) and BL denotes the baseline.

The masses of the outboard motor and the superstructure were not modeled individually; they are included in the total mass, which equals the displacement, and their placement is reflected through the KG and the longitudinal center of gravity of the vessel as a whole given above, whereas the radii of gyration were estimated from empirical ratios. Through these quantities, the masses affect the GM, the natural periods and the accelerations at the evaluation points.

To verify the reverse-engineered geometry, the main dimensions of the drawing were compared with those measured on the scan model, as listed in Table 4. Because the A.P. lies at the outboard motor and not on the hull surface, the length between perpendiculars of the scan model was measured from the A.P. of the drawing to the point where the stem crosses the DLWL; the breadth is the maximum breadth of the scan model, and the depth is the height of the deck edge above the baseline at midship. The differences were 1.1% or less. The length overall of the scan model, 12.27 m, refers to the hull alone, whereas the 14.00 m of the drawing includes the outboard motor bracket. The draft cannot be measured on the hull geometry, so the DLWL of the drawing was placed 0.640 m above the baseline of the scan model. Because the weight and center of gravity of the vessel as built were not measured, the DLWL was determined from the drawing rather than from a balance of weight and buoyancy. At this draft, the displaced volume and the wetted surface area of the scan model in Table 3 were checked in Rhino and used in the analyses. In the resistance analyses, the hull was free to heave and pitch, so its sinkage and trim at each speed were determined by the balance between the weight and the hydrodynamic forces (Section 4.1), whereas the seakeeping analyses used the floating position at the DLWL.

Table 4. Main dimensions in the general arrangement drawing and on the scan model.

Item	Symbol	Drawing	Scan Model	Difference (%)
Length between perpendiculars	L_{BP}	10.12 m	10.11 m	−0.1
Breadth	B	2.84 m	2.81 m	−1.1
Depth	D	0.790 m	0.791 m	+0.1

3. Hydrodynamic Analysis Methods

3.1. Calm-Water Resistance Analysis

Calm-water resistance was evaluated as the baseline hydrodynamic performance of the hull. Although the sea is rarely perfectly calm, the calm-water resistance is the standard reference quantity in ship hydrodynamics because the calm-water analysis determines the required propulsive power and the running attitude at each speed, and the resistance in a seaway is commonly treated as the calm-water resistance plus the added resistance due to waves [19]. The motions of the vessel in waves were evaluated separately in the seakeeping analysis of Section 3.2, whereas the added resistance in waves was not considered in this study. Calm-water resistance was analyzed with Simcenter STAR-CCM+ 2310. The incompressible Reynolds-averaged Navier–Stokes (RANS) equations were solved, the free surface was captured with the volume of fluid (VoF) method [20], and turbulence was modeled with the Reynolds stress transport (RST) model, with the turbulence intensity and turbulent viscosity ratio kept at their default values of 0.01 and 10, respectively. To

capture the running attitude, the hull was free to heave and pitch through the dynamic fluid–body interaction (DFBI) model, and the set-up was configured with reference to the International Towing Tank Conference (ITTC) practical guidelines for ship computational fluid dynamics (CFD) applications [21].

The mesh was generated following the meshing procedure of Yan et al. [22], who determined the grid resolution of a high-speed planing boat with the same solver from a convergence test on three grids; the mesh parameters given below were set for the present hull. As shown in Figure 2e,f, a trimmed mesh aligned with the undisturbed free surface was used, with refinement around the hull, along the free surface and in the Kelvin wave region, and prism layers on the hull surface to resolve the near-wall velocity gradient. The base size was 1 m, giving about 5 million cells in the half-width domain, and six prism layers with a stretching ratio of 1.5 and a total thickness of 0.05 m, or 5% of the base size, were placed on the hull surface. The numerical settings of the resistance analysis are summarized in Table 5.

Table 5. Numerical settings of the resistance analysis in Simcenter STAR-CCM+ 2310.

Item	Setting
Flow model	Incompressible RANS, VoF, RST, first-order convection
Domain	$-3 < X/L_{BP} < 2.5$; $0 < Y/L_{BP} < 1.5$; $-1.5 < Z/L_{BP} < 1.5$
Boundary conditions	Velocity inlet (inlet, top, bottom); pressure outlet (outlet); symmetry (center plane, side); no-slip wall (hull)
Mesh	Trimmed, about 5.0×10^6 cells, base size 1 m; 6 prism layers
Time step	0.01 s
Motion/averaging	Heave and pitch free (two degrees of freedom); mean over converged history

Figure 5 shows the computational domain and boundary conditions. The domain extended over $-3 < X/L_{BP} < 2.5$, $0 < Y/L_{BP} < 1.5$ and $-1.5 < Z/L_{BP} < 1.5$, where X is measured forward from the origin of the hull coordinate system in Figure 4b, Y from the center plane and Z upward from the undisturbed free surface, so that the inlet was located about 1.5 L_{BP} ahead of the F.P. and the outlet about 3 L_{BP} behind the A.P.; the boundaries were thus placed far enough from the hull to avoid blockage effects and wave reflection. A velocity inlet condition was applied at the inlet, top and bottom boundaries, a pressure outlet condition at the downstream boundary and a symmetry condition on both the center plane and the side boundary.

The analysis speeds of 5, 10 and 15 kn (knots; 1 kn = 0.5144 m/s), i.e., 2.57, 5.14 and 7.72 m/s, correspond to length Froude numbers $Fr_L = 0.258$, 0.516 and 0.774 and to volumetric Froude numbers $Fr_\nabla = 0.573$, 1.146 and 1.719. The coefficients of the total resistance R_T, pressure resistance R_P and frictional resistance R_F, together with the two Froude numbers, are defined as follows:

$$C_i = \frac{R_i}{0.5\rho S V^2}, \quad i = \mathrm{T},\ \mathrm{P},\ \mathrm{F} \tag{1}$$

$$Fr_L = \frac{V}{\sqrt{gL_{BP}}}, \quad Fr_\nabla = \frac{V}{\sqrt{g\nabla^{1/3}}} \tag{2}$$

where ρ is the seawater density of 1025 kg/m^3, S is the wetted surface area at rest, V is the ship speed, g is the gravitational acceleration and ∇ is the displaced volume. Resistance and running attitude were taken as mean values over the converged part of the time history after the initial transient.

The time step was set to 0.01 s with reference to the ITTC recommended values, so that the global Courant number remained below 1. For the present speeds, this time step

corresponds to $\Delta t\ V/L_{BP} = 0.0025$, 0.0051 and 0.0076, all of which are below the upper limit of 0.01 recommended in the ITTC guidelines for resistance computations [21].

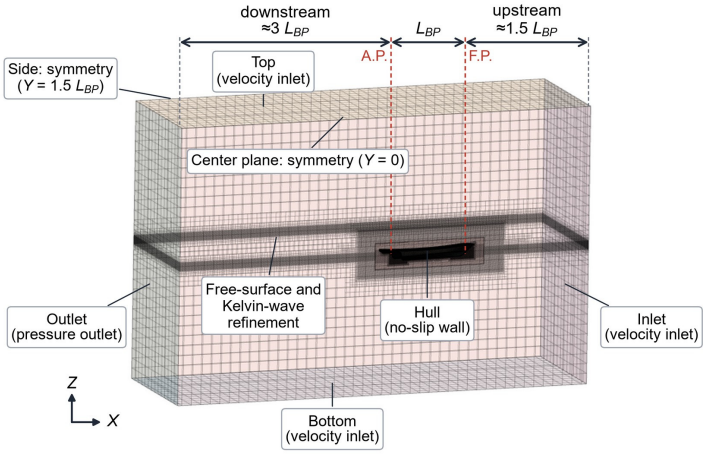


Figure 5. Computational domain and boundary conditions of the resistance analysis.

3.2. Seakeeping Analysis

Seakeeping was analyzed in the frequency domain with ANSYS AQWA 2024 R2, a three-dimensional potential-flow panel code. A mass of 8892 kg, equal to the displacement, was assigned at the center of gravity (COG) of a model consisting of about 6000 panels, and the radii of gyration about the x, y and z axes, k_{xx}, k_{yy} and k_{zz}, were estimated as $0.34B$, $0.25L_{BP}$ and $0.26L_{BP}$, the empirical values for a conventional ship, giving 0.97, 2.53 and 2.63 m, respectively. The response amplitude operators (RAOs) in regular waves were combined with the Pierson–Moskowitz spectrum [23], and the significant single amplitude $2\sqrt{m_0}$ was obtained from the zeroth moment m_0 of the response spectrum. The wave heading β was defined as 0° for following seas, 90° for beam seas and 180° for head seas. As listed in Table 6, a total of 63 conditions combining speeds of 5, 10 and 15 kn, significant wave heights H_s of 0.5, 1.0 and 1.5 m and headings from 0° to 180° in 30° steps were analyzed.

Table 6. Numerical settings of the seakeeping analysis in ANSYS AQWA.

Item	Setting
Method	3D panel method, frequency domain, about 6000 panels
Mass properties	8892 kg at COG (3.029, 0, 0.139) m
Radii of gyration	$k_{xx} = 0.97$ m, $k_{yy} = 2.53$ m, $k_{zz} = 2.63$ m
Wave spectrum	Pierson–Moskowitz, $H_s = 0.5$, 1.0, 1.5 m
Headings	0° (following) to 180° (head), 30° step
Speeds/cases	5, 10, 15 kn/3 × 3 × 7 = 63

The responses in irregular seas were obtained with the linear spectral method [24,25]. For each speed, heading and significant wave height, long-crested irregular waves were represented by the Pierson–Moskowitz spectrum $S_\zeta(\omega)$. The response spectrum S_R of each motion, acceleration or relative motion was obtained from the RAO $H(\omega)$, which is given as a function of the wave frequency ω, and its spectral moments m_n were calculated with the encounter frequency ω_e, given by Equation (7) in Section 4.2, as the weighting variable:

$$S_R(\omega) = |H(\omega)|^2 S_\zeta(\omega), \quad m_n = \int_0^\infty \omega_e^n S_R(\omega) \mathrm{d}\omega \tag{3}$$

where $n = 0$ and 2 are used. Integrating over the wave frequency with ω_e as the weighting variable gives the same moments as integrating the response spectrum over the encounter frequency and remains valid in following and stern-quartering seas, in which ω_e is not a

one-to-one function of ω. The significant single amplitude of a motion or acceleration is $2\sqrt{m_0}$, and the moments m_0 and m_2 of the relative-motion spectra at P3 and P4 are used in Equation (6) to obtain the occurrence rates of deck wetness and slamming.

Because a potential-flow analysis cannot account for viscous damping, damping was incorporated in five steps: (i) RAO analysis without additional damping; (ii) calculation of the natural frequency ω_n and critical damping B_{cr} of each motion mode; (iii) determination of the additional damping B from the damping ratio ζ; (iv) re-analysis of the RAOs with the additional damping applied; and (v) evaluation based on the response spectra. Steps (ii) and (iii) use the following relations:

$$B_{cr} = 2(M + A)\omega_n = \frac{2C}{\omega_n}, \quad B = \zeta B_{cr} \tag{4}$$

$$\zeta(V) = \zeta_0 + (\zeta_{15} - \zeta_0)\frac{V}{15} \tag{5}$$

where M is the mass or mass moment of inertia, A is the added mass, C is the restoring coefficient and V is the ship speed, expressed in kn in Equation (5). Because no damping data were available for the target vessel, the calm-water free-decay values ζ_0 and the corrected 15 kn values ζ_{15} that Kim et al. [26] obtained by combining CFD and a panel method for a 14 m class high-speed coastal rescue boat were adopted and interpolated linearly with speed; the resulting damping ratios are listed in Table 7. The two vessels differ by a factor of about 1.8 in displacement, and their L_{BP}/B ratios are 2.82 for the rescue boat and 3.56 for the target vessel, which introduces uncertainty. The linear interpolation is based on the linear increase in the lift and friction components of roll damping with speed [27]; no equivalent basis exists for heave and pitch.

Table 7. Damping ratios ζ (%) and critical damping B_{cr} applied in the seakeeping analysis.

Mode	0 kn	5 kn	10 kn	15 kn	B_{cr}
Roll, beam seas (90°)	6.0	11.7	17.3	23.0	72,568 N·m·s/rad
Roll, oblique seas (135°)	6.0	10.7	15.3	20.0	72,568 N·m·s/rad
Heave	27.0	28.0	29.0	30.0	213,376 N·s/m
Pitch	11.0	57.3	103.7	150.0	1,075,299 N·m·s/rad

In the procedure of Kim et al. [26], the damping ratio is corrected at the heading and frequency of the largest response spectrum and applied to all headings. For roll, the largest response spectrum occurred in oblique seas at 135° and 1.38 rad/s, and a separate ratio was obtained for beam seas at 90°, because the roll peak frequency there, 2.40 rad/s, differed greatly from that in oblique seas; heave and pitch were corrected in head seas. Accordingly, the roll damping ratios for beam seas in Table 7 were applied at $\beta = 90°$, those for oblique seas at the other six headings of 0°, 30°, 60°, 120°, 150° and 180°, and the heave and pitch ratios at all headings.

Responses were evaluated at the four points on the hull shown in Figure 4b and listed in Table 8: roll and pitch at P1, the center of gravity; vertical and lateral accelerations at P2 in the wheelhouse; deck wetness at P3 on the fore deck; and slamming at P4 on the bottom 0.15 L_{BP} aft of the forward perpendicular. Deck wetness was defined as an event in which the relative motion at P3 exceeds the deck height, and slamming as an event in which the relative motion at P4 exceeds the bottom depth. Assuming the relative motion to be a narrow-band Gaussian process, the number of occurrences per hour N was calculated as follows [19]:

$$N = \frac{3600}{2\pi}\sqrt{\frac{m_2}{m_0}}\exp\left(-\frac{h^2}{2m_0}\right) \tag{6}$$

where m_0 and m_2 are the zeroth and second moments of the relative-motion response spectrum, and h is the critical relative displacement, namely the deck height at P3 and the bottom depth at P4. Ochi [28] defined slamming as bottom emergence accompanied by a relative velocity exceeding a threshold value. The present study did not apply the relative-velocity condition and counted bottom emergence only.

Table 8. Response evaluation points and seakeeping criteria.

Point	(x, y, z) (m)	Response	Operational	Survival
P1 (COG)	(3.03, 0, 0.14)	Roll (deg)	8.0	30.0
P1 (COG)	(3.03, 0, 0.14)	Pitch (deg)	4.8	8.0
P2 (wheelhouse)	(1.89, 0, 0.92)	Vertical acceleration (g)	0.4	0.8
P2 (wheelhouse)	(1.89, 0, 0.92)	Lateral acceleration (g)	0.2	0.4
P3 (fore deck)	(9.56, 0, 0.90)	Deck wetness (1/h)	30	50
P4 (bottom, 0.15 L_{BP})	(6.99, 0, −0.55)	Slamming (1/h)	20	50

3.3. Seakeeping Criteria

The computed responses were assessed against the operational and survival limits listed in Table 8. Seakeeping assessments of fishing vessels use criteria for deck wetness and slamming in addition to those for motions and accelerations [29]. The limit values are those that Kim et al. [26] applied to a high-speed coastal rescue boat on the basis of naval-vessel criteria, namely the seakeeping design guideline of the Republic of Korea Navy and the criteria of NORDFORSK [30] and NATO [31]. The operational limit was interpreted as the limit up to which normal navigation and work remain possible, and the survival limit as the limit at which the safety of the hull and crew begins to be threatened. The criteria cover three aspects of operation: motions, accelerations and the frequency of water-on-deck and bottom-emergence events. Roll and pitch at the center of gravity represent the overall motion of the hull, which affects stability, the handling of fishing gear and the safety of the crew on deck. The vertical and lateral accelerations are evaluated at the wheelhouse, where the vessel is operated; the vertical acceleration is related to motion sickness and to the ability of the crew to work, whereas the lateral acceleration, to which sway, roll and yaw all contribute, is related to the loss of balance of persons and the sliding of objects. Roll, pitch and the accelerations are compared with the limits as significant single amplitudes, whereas deck wetness at the fore deck and slamming at the bottom 0.15 L_{BP} aft of the forward perpendicular are compared as numbers of occurrences per hour obtained from Equation (6).

4. Results and Discussion

4.1. Calm-Water Resistance and Flow Field

Figure 6 shows the time histories of the total and pressure resistance coefficients, from which the mean values were obtained. At 5 kn (2.57 m/s), the coefficients oscillate regularly before settling around their means, with a peak-to-peak amplitude of about 5% of the mean total coefficient over the last 40 s of the record; at 10 kn the oscillation is about 1%, and at 15 kn the coefficients are practically constant. The oscillation amplitude gives an indication of the iterative uncertainty of these mean values.

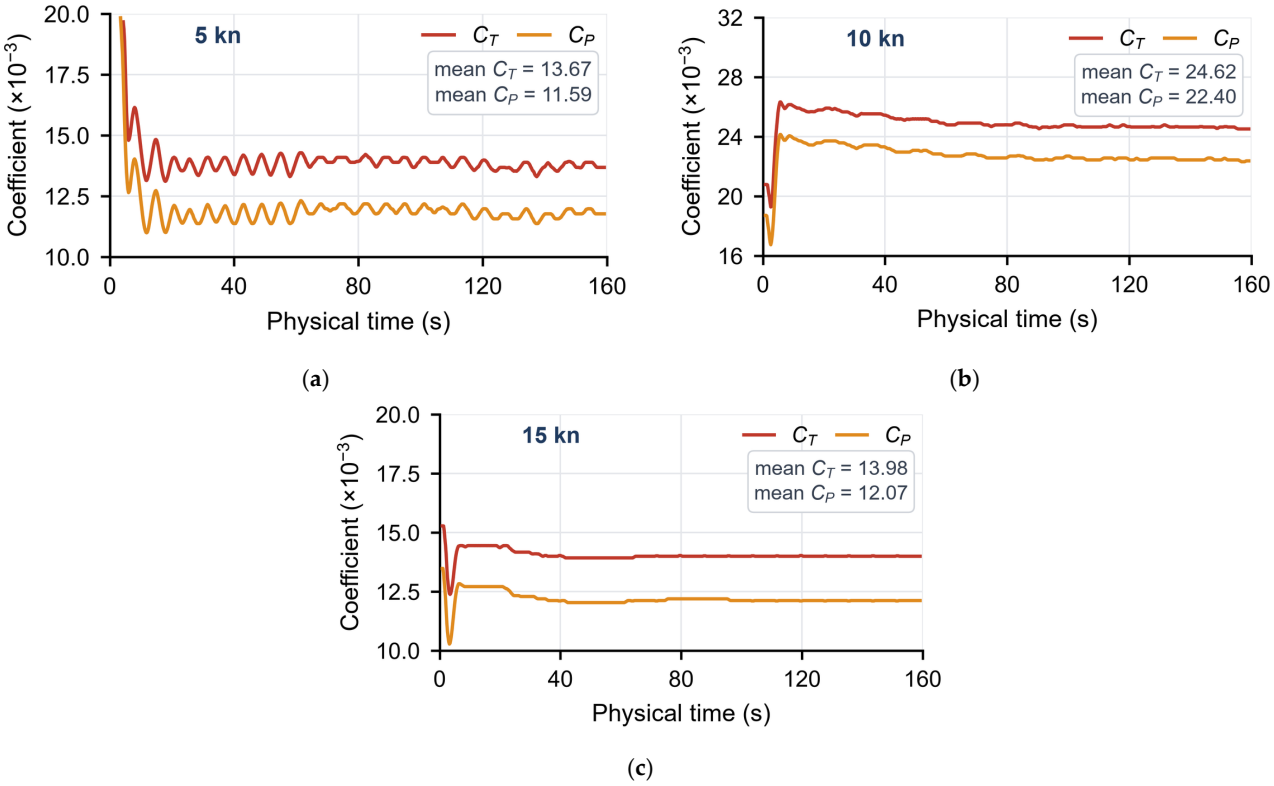


Figure 6. Time histories of the total resistance coefficient C_T and pressure resistance coefficient C_P of the target vessel: (**a**) 5 kn; (**b**) 10 kn; (**c**) 15 kn.

Table 9 and Figure 7 summarize the calm-water resistance results for the target vessel. The total resistance R_T at 5, 10 and 15 kn was 1502, 10,822 and 13,832 N, respectively, and the corresponding effective power, $P_E = R_T V$, was 3.9, 55.7 and 106.7 kW. When the speed doubled from 5 to 10 kn, R_T increased by a factor of 7.2, corresponding to $R_T \propto V^{2.85}$, whereas from 10 to 15 kn it increased by a factor of only 1.28, corresponding to $R_T \propto V^{0.61}$. Because each component was averaged separately, $R_P + R_F$ differs from R_T by at most 7 N. With a kinematic viscosity of $\nu = 1.1892 \times 10^{-6}$ m^2/s for seawater at 15 °C, the Reynolds number based on L_{BP} ranges from 2.19×10^7 to 6.57×10^7. The ratio $R_T/(\Delta g)$ increases from 0.017 to 0.159 with the transition from the displacement to the semi-displacement regime.

Table 9. Calm-water resistance of the target vessel.

Quantity	5 kn	10 kn	15 kn
Fr_L/Fr_∇	0.258/0.573	0.516/1.146	0.774/1.719
R_T (N)	1502	10,822	13,832
R_P (N)	1274	9849	11,941
R_F (N)	229	973	1884
C_T (×10^{-3})	13.67	24.62	13.98
C_P (×10^{-3})	11.59	22.40	12.07
C_F (×10^{-3})	2.08	2.21	1.90
P_E (kW)	3.9	55.7	106.7
Trim (deg, bow up)	0.21	3.78	5.62
Heave (mm, positive upward)	−12	−44	−45

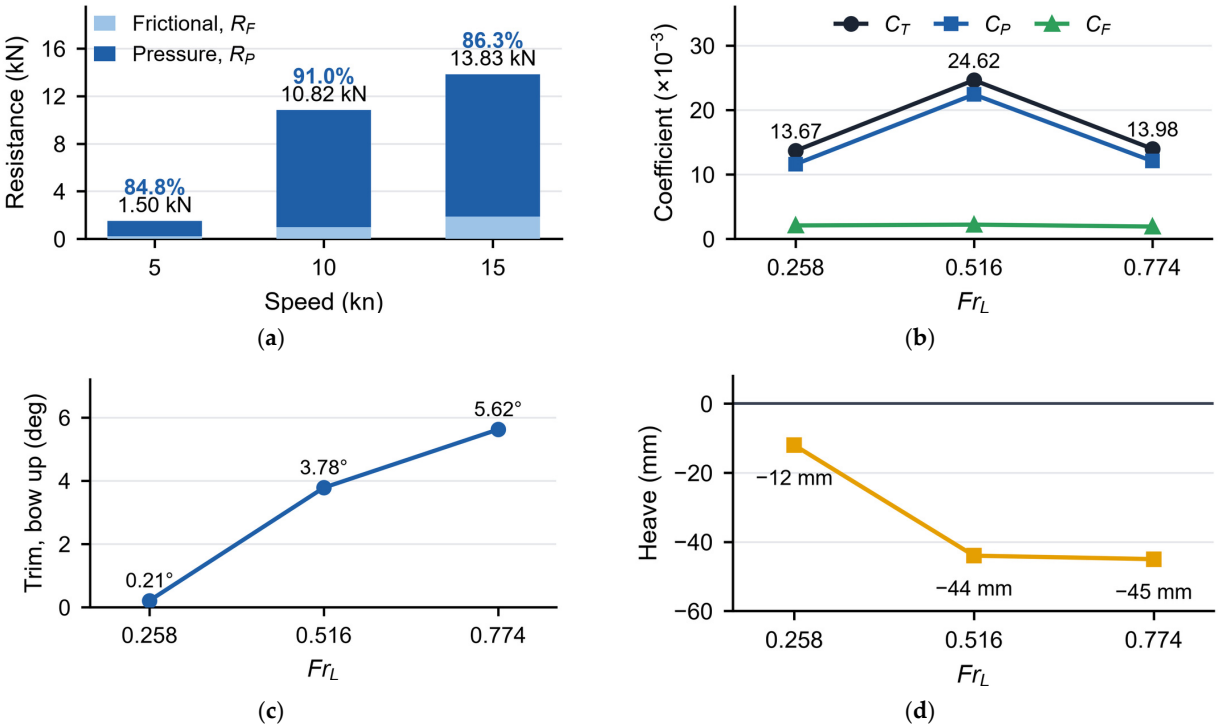


Figure 7. Calm-water resistance and running attitude of the target vessel: (**a**) resistance components, with the total resistance and the share of the pressure resistance in it above each bar; (**b**) resistance coefficients; (**c**) dynamic trim; (**d**) heave, positive upward.

As shown in Figure 7a, the pressure resistance R_P accounted for 85–91% of R_T at all speeds, and the frictional resistance R_F for the remaining 9–15%. A substantial part of R_P is the component associated with the dynamic trim angle τ; approximated as $\Delta g \tan \tau$, this component amounts to about 5.8 kN at 10 kn and about 8.6 kN at 15 kn [32]. Trim control, in addition to hull-form improvement, can therefore be expected to be effective in reducing the resistance.

As shown in Figure 7b, the total resistance coefficient C_T was 13.67 × 10^{-3}, 24.62 × 10^{-3} and 13.98 × 10^{-3} at Fr_L = 0.258, 0.516 and 0.774, respectively, and was thus largest at the intermediate speed. Length Froude numbers above about 0.4–0.5 correspond to the semi-displacement regime, in which dynamic pressure begins to contribute to supporting the hull [32]; the target vessel therefore operates in this regime from 10 kn upward.

The running attitude in Figure 7c,d reflects the same change in regime. The bow-up dynamic trim angle increased from 0.21° to 3.78° and 5.62°, whereas the hull sank by 12, 44 and 45 mm; that is, the sinkage changed little between 10 and 15 kn.

Figure 8 shows the free-surface elevation around the hull. At 5 kn, transverse waves shorter than the hull were generated, with a wavelength of about 4.2 m. At 10 kn, the transverse wavelength increased to about 16.9 m, approximately 1.7 times L_{BP}, so that a wave trough formed at the stern and a crest further aft. At 15 kn, divergent waves dominated the wave pattern.

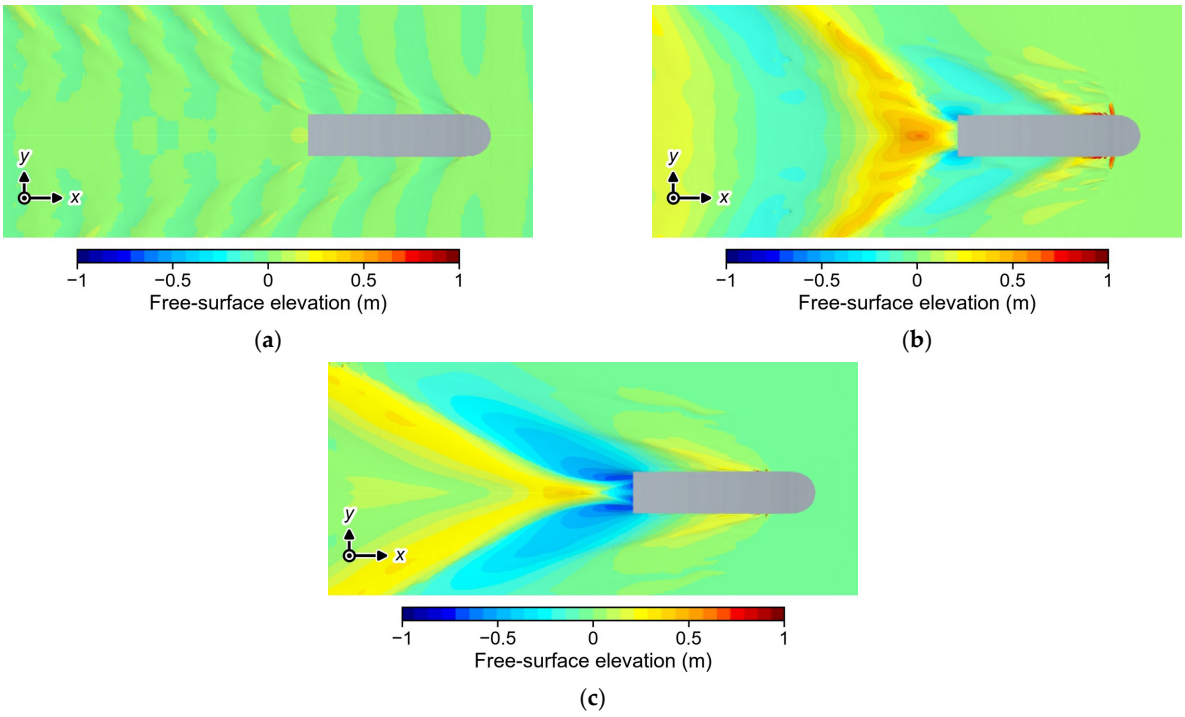


Figure 8. Free-surface elevation around the target vessel: (**a**) 5 kn, $Fr_L = 0.26$; (**b**) 10 kn, $Fr_L = 0.52$; (**c**) 15 kn, $Fr_L = 0.77$.

The corresponding distributions of the local pressure coefficient C_p on the hull bottom are shown in Figure 9. At 5 kn, the entire bottom was wetted. At 10 kn, a low-pressure region appeared at the stern step. At 15 kn, the high-pressure region on the bottom shifted aft and the forebody bottom emerged from the water, which is consistent with semi-displacement behavior.

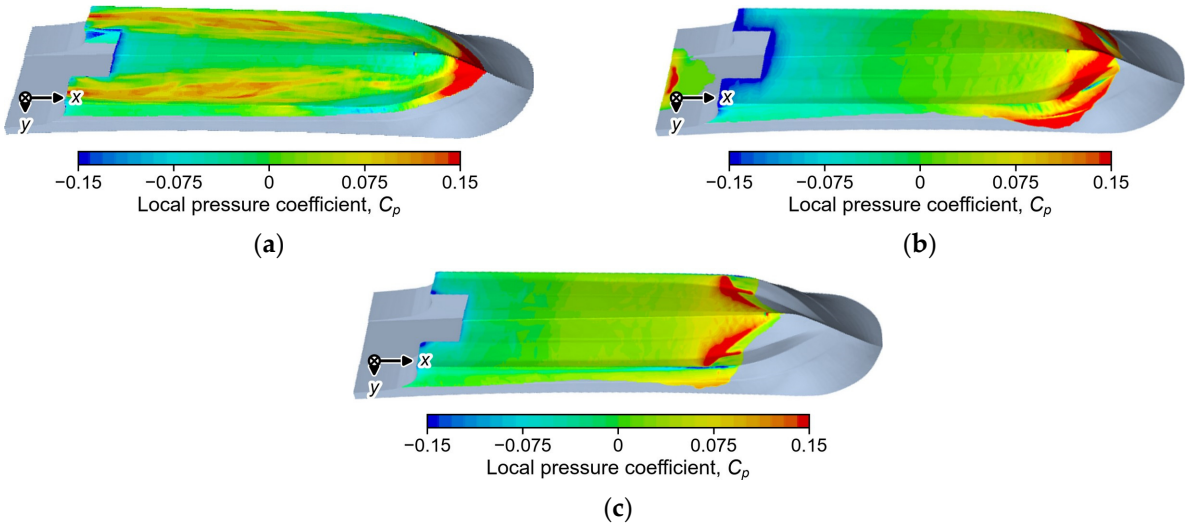


Figure 9. Local pressure coefficient C_p on the hull bottom of the target vessel: (**a**) 5 kn; (**b**) 10 kn; (**c**) 15 kn.

4.2. Motion Response Amplitude Operators

Figure 10 shows the roll and pitch RAOs at the center of gravity at 10 kn. The roll RAO reaches a maximum of about 12°/m near wave frequencies of 2.0–2.3 rad/s at $\beta = 60°$ and 90°, that is, in stern-quartering and beam seas, whereas it is nearly zero in following and head seas. The pitch RAO exhibits narrow peaks of about 12°/m and 14°/m at about 1.9

and 2.2 rad/s for $\beta = 0°$ and 30°, respectively. For a ship advancing with forward speed, the encounter frequency of a wave with heading β and wave frequency ω is given by the well-known relation [24,25]

$$\omega_e = \omega - \frac{\omega^2 V}{g}\cos\beta \tag{7}$$

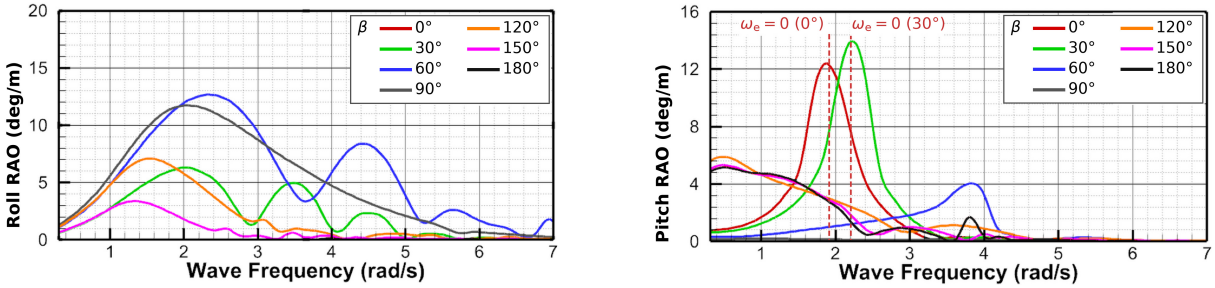


Figure 10. Motion RAOs at the center of gravity of the target vessel at 10 kn: (**a**) roll; (**b**) pitch. The dashed lines in (**b**) mark $\omega_e = 0$ for $\beta = 0°$ and 30°.

For $|\beta| < 90°$, that is, in following and stern-quartering seas, Equation (7) yields $\omega_e = 0$ at $\omega = g/(V\cos\beta)$. At 10 kn, this frequency is 1.91, 2.20 and 3.81 rad/s for $\beta = 0°$, 30° and 60°, respectively, and lies close to the pitch peaks in Figure 10b, including the minor peak near 3.8 rad/s at 60°. The peaks at 0° and 30° therefore represent a quasi-static response: the phase velocity of the waves equals the component of the ship speed in the wave direction, and the hull follows the surface slope of waves 12.7–16.9 m long, or 1.3–1.7 times L_{BP}. At 15 kn, the peaks likewise shifted to the vicinity of $\omega_e = 0$, which lies at 1.27, 1.47 and 2.54 rad/s for $\beta = 0°$, 30° and 60°, respectively.

The International Maritime Organization (IMO) guidance to masters [33] identifies a surf-riding/broaching danger zone for encounter angles $135° < \alpha < 225°$ at speeds above $1.8\sqrt{L_{BP}}/\cos(180°-\alpha)$ kn, where α is the encounter angle measured from head seas and is related to the wave heading used here by $\alpha = 180° - \beta$; for the target vessel in direct following seas, where $\alpha = 180°$, this threshold is about 5.7 kn.

4.3. Responses in Irregular Waves and Criteria Assessment

The responses in irregular waves were obtained from the RAOs at each heading and the Pierson–Moskowitz spectrum by the spectral method described in Section 3.2. Table 10 and Figure 11 present the maximum responses over all wave headings for the nine combinations of three speeds and three significant wave heights, denoted below as speed/significant wave height, for example, 15 kn/1.5 m. Roll reached a maximum of 6.26° at 15 kn/1.5 m and satisfied the 8° operational limit in all conditions. Pitch exceeded the 4.8° operational limit at 10 kn/1.5 m and 15 kn/1.0 m and reached 8.05° at 15 kn/1.5 m, exceeding the 8.0° survival limit. All of these pitch maxima occurred in following seas, where the encounter frequency approaches zero; at 10 and 15 kn, these conditions also lie in the surf-riding/broaching danger zone noted in Section 4.2. Pitch in head seas remained within the operational limit in all conditions, whereas the results for individual headings, which are not presented here, show that at 15 kn/1.5 m pitch exceeded the operational limit at every heading from 0° to 120°. Vertical acceleration exceeded the 0.4 g operational limit at 10 kn/1.5 m, 15 kn/1.0 m and 15 kn/1.5 m. Lateral acceleration exceeded the 0.2 g operational limit in eight of the nine conditions and reached 0.41 g at 15 kn/1.5 m, beyond the survival limit.

Table 10. Maximum responses over all wave headings, given as significant single amplitudes and, for deck wetness and slamming, as occurrence rates.

V (kn)	H_s (m)	Roll (deg)	Pitch (deg)	a_v (g)	a_h (g)	Deck Wetness (1/h)	Slamming (1/h)
Operational/ survival limit		8.0/30.0	4.8/8.0	0.4/0.8	0.2/0.4	30/50	20/50
5	0.5	2.48	1.93	0.16	0.20	0.8	0.0
5	1.0	4.38	3.11	0.28	**0.29**	**32.0**	0.2
5	1.5	5.60	3.55	0.37	**0.34**	**60.7**	0.6
10	0.5	2.64	2.92	0.18	**0.21**	3.7	7.7
10	1.0	4.61	3.64	0.38	**0.31**	**93.0**	**60.0**
10	1.5	5.93	**5.57**	**0.52**	**0.38**	**154.8**	**89.5**
15	0.5	3.31	3.34	0.22	**0.22**	13.1	**80.3**
15	1.0	5.16	**5.91**	**0.46**	**0.34**	**193.6**	**246.2**
15	1.5	6.26	**8.05**	**0.64**	**0.41**	**297.7**	**286.0**

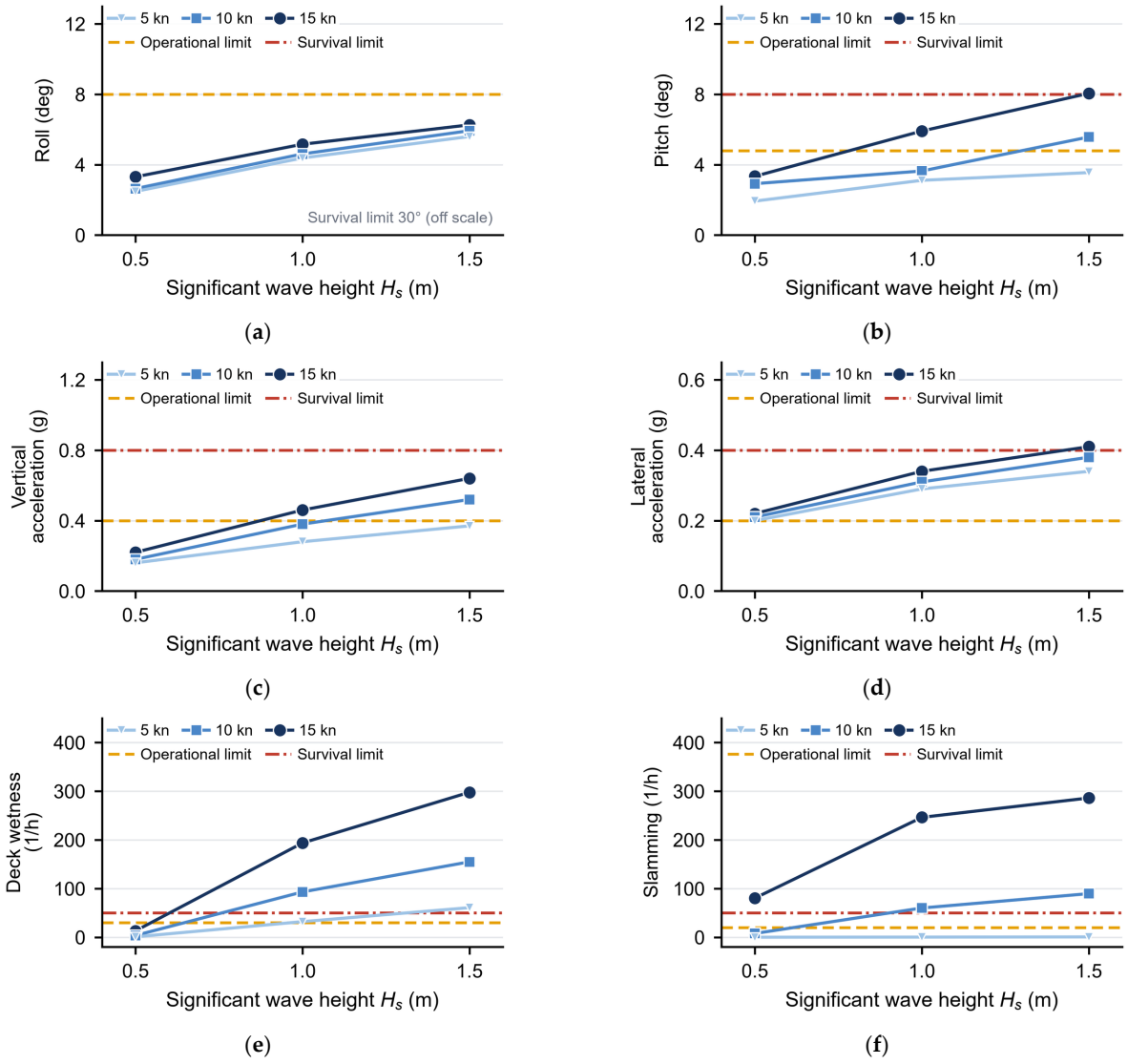


Figure 11. Maximum responses of the target vessel over all wave headings compared with the operational and survival limits: (**a**) roll; (**b**) pitch; (**c**) vertical acceleration; (**d**) lateral acceleration; (**e**) deck wetness; (**f**) slamming.

In Table 10, a_v and a_h denote the vertical and lateral accelerations at P2, and slamming is counted as bottom emergence; values exceeding an operational limit are printed in bold, and a value equal to a limit is regarded as satisfying it. The maxima occurred at headings of 60–90° for roll, 90° for the lateral acceleration, 0° for pitch, 120–180° for the vertical acceleration and 180° for deck wetness and slamming.

Deck wetness remained within the operational limit of 30 events/h at $H_s = 0.5$ m, with a maximum of 13.1 events/h, but at $H_s = 1.0$ m it exceeded this limit even at 5 kn, reaching 32.0 events/h. It also exceeded the 50 events/h survival limit at 5 kn/1.5 m, where it reached 60.7 events/h, and at 10 and 15 kn with $H_s \geq 1.0$ m, reaching 297.7 events/h at 15 kn/1.5 m. Slamming exceeded the survival limit of 50 events/h at 10 kn with $H_s \geq 1.0$ m, at rates of 60.0 and 89.5 events/h, and at 15 kn at all wave heights analyzed, already reaching 80.3 events/h at $H_s = 0.5$ m; thus, at high speed, bottom emergence occurred frequently even in relatively mild seas.

With a metacentric height GM of 1.111 m, corresponding to $GM/B \approx 0.39$, the target vessel has high initial stability, which, with the roll damping ratios assumed in Table 7, kept the roll angles small: the maximum of 6.26° was about 22% below the 8° operational limit. However, the lateral acceleration at the wheelhouse exceeded the operational limit in eight of the nine conditions. Because the roll angles are small and the wheelhouse evaluation point P2 lies only 0.78 m above the center of gravity, the lateral acceleration induced there by the largest roll of 6.26° at the roll RAO peak frequencies of 2.0–2.3 rad/s shown in Figure 10a is less than 0.16 g even when the gravity component due to the heel angle is included, whereas the computed value reaches 0.41 g; the lateral acceleration therefore arises mainly from the sway and yaw motions. In addition, the deck at the deck-wetness evaluation point P3 is only 0.90 m above the waterline, so the relative motion of the bow readily produced deck wetness. For a 9.77 GT class fishing vessel, Choi et al. [1] found roll to be the governing response, exceeding the operational limit from $H_s = 0.4$ m, which indicates that the response restricting operation can differ with hull form and stability characteristics. Mata-Álvarez-Santullano and Souto-Iglesias [34] also reported that the stability and operability of small fishing vessels do not necessarily coincide.

4.4. Operability Envelope

Figure 12 summarizes the assessment of the six criteria on the speed–significant wave height plane. Of the nine conditions, only 5 kn/0.5 m satisfies all operational limits, and even in this condition the lateral acceleration of 0.20 g equals the operational limit, leaving no margin. At $H_s = 0.5$ m, speeds of 10 kn or higher already exceed the lateral-acceleration or slamming limit, and at $H_s = 1.0$ m, deck wetness and lateral acceleration exceed their operational limits even at 5 kn, the lowest speed analyzed, reaching 32.0 events/h and 0.29 g, respectively.

A wind–wave advisory is issued when sea-surface wind speeds of 14 m/s or more are expected to persist for 3 h or longer, or when significant wave heights of 3 m or more are expected [35]. Because the target vessel already exceeds the operational limits at far lower significant wave heights, such hull-specific operability limits can serve as a basis for complementing the current departure restrictions, which are defined mainly by gross tonnage ranges. However, at 5 kn/1.0 m, the deck-wetness limit is exceeded by only about 7%, whereas the lateral-acceleration limit is exceeded by about 45%; both results depend on the assumed damping ratios and wave spectrum. Sensitivity analyses and validation against full-scale measurements are therefore required before $H_s = 1.0$ m is applied as a criterion for operational decisions.

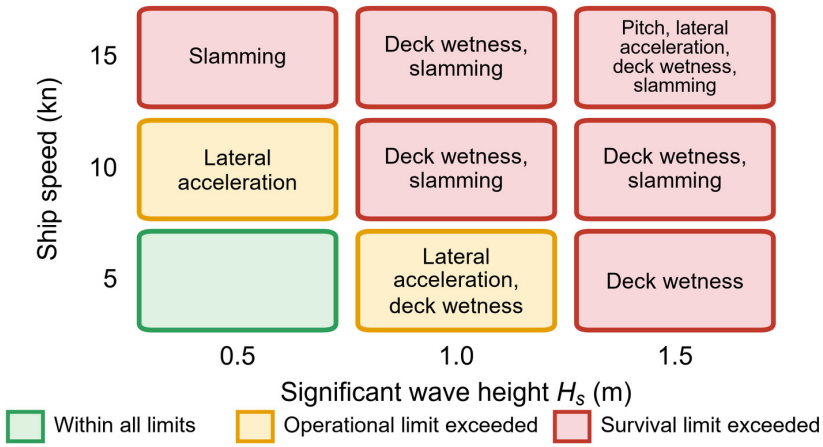


Figure 12. Operability map of the target vessel. The cell color shows the highest limit level exceeded.

The procedure and the hull-specific operability limits presented here are planned to be proposed for incorporation into the qualification procedures for small fishing vessels and the related safety standards. To this end, the procedure will be applied to the representative vessels of each tonnage class to establish a hull-form–performance database, the accuracy requirements of the scan-to-analysis procedure will be standardized, and the results will be validated against model tests and full-scale measurements. The procedure could then be included in the qualification procedures that check whether a vessel meets the safety regulations, for example, to identify newly built or modified vessels whose hull forms deviate substantially from the representative hull form of their tonnage class and therefore require an individual assessment. The hull-specific operability limits could also be reflected in the safety standards, such as the departure restrictions, which are currently classified by gross tonnage.

5. Conclusions

This study established a reverse-engineering procedure based on 3D laser scanning for Korean coastal fishing vessels, for which design data are scarce, and applied it to a 3 GT class coastal fishing vessel to assess its resistance, seakeeping performance and operability limits. The main conclusions are as follows.

1. In the sample of 21 vessels selected from the 2391 fishing vessels that passed construction survey in 2023–2025, L/B differed by up to 1.49 even within the same tonnage class; tonnage alone is therefore insufficient to represent the hull form.
2. A measurement-to-analysis procedure was established in which check items are assigned to the field scanning, post-processing, reverse-engineering and hydrodynamic-analysis stages, and corrective actions to the first three of them. Reversal of the surface orientation when a mold is scanned, coordinate alignment based on reference planes, watertight-surface correction and appendage removal are the key steps in generating an analysis model.
3. Among the three speeds analyzed, the total resistance coefficient of the target vessel was largest at $Fr_{\mathrm{L}} = 0.516$, where it reached 24.62×10^{-3}, and the pressure resistance accounted for 85–91% of the total resistance. At 10 kn and above, the increasing trim, the leveling-off of the sinkage and the aft shift in the high-pressure region on the hull bottom indicated a transition to the semi-displacement regime, and a substantial part of the pressure resistance was attributable to the dynamic trim.
4. Across the nine combinations of speed and significant wave height, the maximum roll angle over all headings was 6.26°, within the operational limit. In contrast, the

lateral acceleration exceeded the operational limit in eight combinations, deck wetness did so from $H_s = 1.0$ m, and pitch in following seas and the vertical acceleration did so at 10 kn/1.5 m and at 15 kn with $H_s \geq 1.0$ m. The survival limit was exceeded by slamming, counted as bottom emergence, at 10 kn with $H_s \geq 1.0$ m and at 15 kn for all wave heights analyzed, by deck wetness at 5 kn/1.5 m and at 10 and 15 kn with $H_s \geq 1.0$ m, and by pitch and lateral acceleration at 15 kn/1.5 m. Only the combination of 5 kn and $H_s = 0.5$ m satisfied all operational limits, and at $H_s = 1.0$ m the limits were exceeded even when the speed was reduced to 5 kn.

5. Owing to its large GM, the target vessel exhibited small roll angles. Nevertheless, the lateral acceleration in the wheelhouse was large; because the roll angles are small and the wheelhouse lies only 0.78 m above the center of gravity, this acceleration arises mainly from sway and yaw. In addition, the low deck height made deck wetness occur readily. For the roll damping ratios assumed in Table 7, the operability limits are thus determined not by the roll angle but by the lateral acceleration and the relative motion at the bow, so stability indices alone are insufficient to judge operational safety. Hull-specific operability limits derived from measured geometry can serve as supporting data that complement the current departure restrictions, which are based mainly on gross tonnage ranges.

Future work will apply the same procedure to the other representative vessels in Table 2 to build a hull-form–performance database for each tonnage class, and will verify the present results through a free-decay analysis of the target vessel, seakeeping analyses that account for the running attitude, sensitivity analyses of the damping ratios and evaluation criteria, model tests and full-scale measurements.

Author Contributions: Conceptualization, S.S. and D.S.; methodology, M.M., S.S., J.O. and D.S.; software, M.M.; validation, M.M., S.S. and J.O.; formal analysis, M.M., S.S. and D.S.; investigation, M.M. and S.S.; resources, S.S., S.K. and D.S.; data curation, M.M.; writing—original draft preparation, M.M.; writing—review and editing, S.S., J.O., S.K. and D.S.; visualization, M.M.; supervision, D.S.; project administration, S.S., S.K. and D.S.; funding acquisition, S.S., S.K. and D.S. All authors have read and agreed to the published version of the manuscript.

Funding: This research was supported by the Korea Maritime Transportation Safety Authority, funded by the project "Study on Reverse Engineering of Coastal Fishing Vessel Hulls and Hydrodynamic Performance Analysis Using a 3D Scanner" and by the Korea Institute of Marine Science & Technology Promotion (KIMST), funded by the Ministry of Oceans and Fisheries, Korea (RS-2023-00256122).

Data Availability Statement: The original contributions presented in this study are included in the article. Further inquiries can be directed to the corresponding authors.

Conflicts of Interest: The authors declare no conflicts of interest.

References

1. Choi, G.-Y.; Song, C.-U.; Park, Y.-S.; Park, J.-B. Basic study to establish marine activity criteria based on the seakeeping performance of less than 10-tons fishing vessels (I). *J. Korean Soc. Mar. Environ. Saf.* **2022**, *28*, 965–972. [CrossRef]
2. Korea Maritime Safety Tribunal. Marine Accident Statistics. Available online: https://www.kmst.go.kr/web/page.do?menuIdx=125 (accessed on 16 October 2026).
3. Ministry of Oceans and Fisheries. Enforcement Rule of the Act on Safe Operation of Fishing Vessels and Promotion of Safety and Health of Crew Members, Article 4. Available online: https://www.law.go.kr (accessed on 16 October 2026).
4. Im, N.-K.; Lee, S.-M. A study on motion response of small fishing vessels according to various tonnage in regular waves. *J. Korean Soc. Mar. Environ. Saf.* **2021**, *27*, 832–838. [CrossRef]
5. Lee, D.-K.; Park, B.-Y. A method of geometry and weight quality control for composite small crafts using a handheld-type 3D scanner. *J. Korean Soc. Mech. Technol.* **2020**, *22*, 545–552. [CrossRef]

6. Gim, E.-C.; Jung, K.-S.; Park, B.-Y.; Lee, D.-K. Environmental impact assessment and sustainable design method for a composit small craft using 3D scanning-based reverse-engineered model. *J. Korean Soc. Mar. Environ. Saf.* **2025**, *31*, 520–529. [CrossRef]
7. Bartoš, K.; Pukanská, K.; Repáň, P.; Kseňak, Ľ.; Sabová, J. Modelling the surface of racing vessel's hull by laser scanning and digital photogrammetry. *Remote Sens.* **2019**, *11*, 1526. [CrossRef]
8. Burdziakowski, P.; Tysiac, P. Combined close range photogrammetry and terrestrial laser scanning for ship hull modelling. *Geosciences* **2019**, *9*, 242. [CrossRef]
9. Edessa, D.M.; Bronsart, R. A contribution to curves network based ship hull form reverse engineering. *Int. Shipbuild. Prog.* **2015**, *62*, 17–42. [CrossRef]
10. Lovas, T.; Somogyi, Á.J.; Simongáti, G. Laser scanning ship hulls to support hydrodynamic simulations. *Period. Polytech. Civ. Eng.* **2022**, *66*, 291–297. [CrossRef]
11. Park, D.-W.; Lee, K.; Seo, J. Evaluation of the seakeeping performance indices for enhancing crew safety and workability in small fishing vessels. *J. Ocean Eng. Technol.* **2024**, *38*, 336–349. [CrossRef]
12. Gaglione, S.; Piscopo, V.; Scamardella, A. The overall motion induced interruptions as operability criterion for fishing vessels. *J. Mar. Sci. Technol.* **2016**, *21*, 517–532. [CrossRef]
13. Iqbal, M.; Terziev, M.; Tezdogan, T.; Incecik, A. Operability analysis of traditional small fishing boats in Indonesia with different loading conditions. *Ships Offshore Struct.* **2023**, *18*, 1060–1079. [CrossRef]
14. Cakici, F.; Aydin, M. Effects of hull form parameters on seakeeping for YTU gulet series with cruiser stern. *Int. J. Nav. Archit. Ocean Eng.* **2014**, *6*, 700–714. [CrossRef]
15. De Luca, F.; Mancini, S.; Miranda, S.; Pensa, C. An extended verification and validation study of CFD simulations for planing hulls. *J. Ship Res.* **2016**, *60*, 101–118. [CrossRef]
16. Wheeler, M.P.; Matveev, K.I.; Xing, T. Numerical study of hydrodynamics of heavily loaded hard-chine hulls in calm water. *J. Mar. Sci. Eng.* **2021**, *9*, 184. [CrossRef]
17. Oyuela, S.; Díaz Ojeda, H.R.; Pérez Arribas, F.; Otero, A.D.; Sosa, R. Investigating fishing vessel hydrodynamics by using EFD and CFD tools, with focus on total ship resistance and its components. *J. Mar. Sci. Eng.* **2024**, *12*, 622. [CrossRef]
18. Iqbal, M.; Terziev, M.; Tezdogan, T.; Incecik, A. Hull form optimisation to minimise the total resistance and dynamic responses of small fishing vessels. *Ocean Eng.* **2025**, *321*, 120357. [CrossRef]
19. Faltinsen, O.M. *Sea Loads on Ships and Offshore Structures*; Cambridge University Press: Cambridge, UK, 1990.
20. Tezdogan, T.; Demirel, Y.K.; Kellett, P.; Khorasanchi, M.; Incecik, A.; Turan, O. Full-scale unsteady RANS CFD simulations of ship behaviour and performance in head seas due to slow steaming. *Ocean Eng.* **2015**, *97*, 186–206. [CrossRef]
21. ITTC. *Practical Guidelines for Ship CFD Applications*; Recommended Procedures and Guidelines 7.5-03-02-03; International Towing Tank Conference: Zürich, Switzerland, 2014.
22. Yan, K.; Oh, J.; Seo, D.-W. Numerical study on the performance of resistance various trim tab's position and size for high-speed small boat. *J. Korea Acad.-Ind. Coop. Soc.* **2023**, *24*, 206–218. [CrossRef]
23. Pierson, W.J.; Moskowitz, L. A proposed spectral form for fully developed wind seas based on the similarity theory of S. A. Kitaigorodskii. *J. Geophys. Res.* **1964**, *69*, 5181–5190. [CrossRef]
24. Lewis, E.V. (Ed.) *Principles of Naval Architecture*, 2nd ed.; Society of Naval Architects and Marine Engineers: Jersey City, NJ, USA, 1989; Volume III, Motions in Waves and Controllability.
25. Lloyd, A.R.J.M. *Seakeeping: Ship Behaviour in Rough Weather*; Ellis Horwood: Chichester, UK, 1989.
26. Kim, Y.-R.; Park, J.-B.; Park, J.-C.; Park, S.-K.; Lee, W.-M. Development of an evaluation procedure for seakeeping performance of high-speed planing hull using hybrid method. *J. Soc. Nav. Archit. Korea* **2019**, *56*, 200–210. [CrossRef]
27. ITTC. *Estimation of Roll Damping*; Recommended Procedures and Guidelines 7.5-02-07-04.5; International Towing Tank Conference: Zürich, Switzerland, 2021.
28. Ochi, M.K. Prediction of occurrence and severity of ship slamming at sea. In Proceedings of the 5th Symposium on Naval Hydrodynamics, Bergen, Norway, 10–12 September 1964; Office of Naval Research: Washington, DC, USA, 1966; pp. 545–596.
29. Tello, M.; Ribeiro e Silva, S.; Guedes Soares, C. Seakeeping performance of fishing vessels in irregular waves. *Ocean Eng.* **2011**, *38*, 763–773. [CrossRef]
30. NORDFORSK. *Assessment of Ship Performance in a Seaway*; Nordic Cooperative Project: Seakeeping Performance of Ships; NORDFORSK: Copenhagen, Denmark, 1987.
31. NATO. *Common Procedures for Seakeeping in the Ship Design Process*, 3rd ed.; STANAG 4154; North Atlantic Treaty Organization: Brussels, Belgium, 2000.
32. Faltinsen, O.M. *Hydrodynamics of High-Speed Marine Vehicles*; Cambridge University Press: Cambridge, UK, 2005.
33. International Maritime Organization. *Revised Guidance to the Master for Avoiding Dangerous Situations in Adverse Weather and Sea Conditions*; MSC.1/Circ.1228; IMO: London, UK, 2007.

34. Mata-Álvarez-Santullano, F.; Souto-Iglesias, A. Stability, safety and operability of small fishing vessels. *Ocean Eng*. **2014**, *79*, 81–91. [CrossRef]
35. Korea Meteorological Administration. Marine Weather Warnings. Available online: https://www.weather.go.kr/w/ocean/warning.do (accessed on 16 October 2026).

Disclaimer/Publisher's Note: The statements, opinions and data contained in all publications are solely those of the individual author(s) and contributor(s) and not of MDPI and/or the editor(s). MDPI and/or the editor(s) disclaim responsibility for any injury to people or property resulting from any ideas, methods, instructions or products referred to in the content.